ACS NANO

www.acsnano.org

ARTICLE

Realization of Epitaxial NbP and TaP Weyl Semimetal Thin Films

Amilcar Bedoya-Pinto,* Avanindra Kumar Pandeya, Defa Liu, Hakan Deniz, Kai Chang, Hengxin Tan, Hyeon Han, Jagannath Jena, Ilya Kostanovskiy, and Stuart S. P. Parkin*

Cite This: *ACS Nano* 2020, 14, 4405–4413

Read Online

ACCESS | Metrics & More | Article Recommendations | Supporting Information

ABSTRACT: **Weyl semimetals (WSMs) exhibit an electronic structure governed by linear band dispersions and degenerate (Weyl) points that lead to exotic physical phenomena. While WSMs were established in bulk monopnictide compounds several years ago, the growth of thin films remains a challenge. Here, we report the bottom-up synthesis of single-crystalline NbP and TaP thin films, 9 to 70 nm thick, by means of molecular beam epitaxy. The as-grown epitaxial films feature a phosphorus-rich stoichiometry, a tensile-strained unit cell, and a homogeneous surface termination, unlike their bulk crystal counterparts. These properties result in an electronic structure governed by topological surface states as directly observed using *in situ* momentum photoemission microscopy, along with a Fermi-level shift of −0.2 eV with respect to the intrinsic chemical potential. Although the Fermi energy of the as-grown samples is still far from the Weyl points, carrier mobilities close to 10^3 $cm^2/(V\ s)$ have been measured at room temperature in patterned Hall-bar devices. The ability to grow thin films of Weyl semimetals that can be tailored by doping or strain, is an important step toward the fabrication of functional WSM-based devices and heterostructures.**

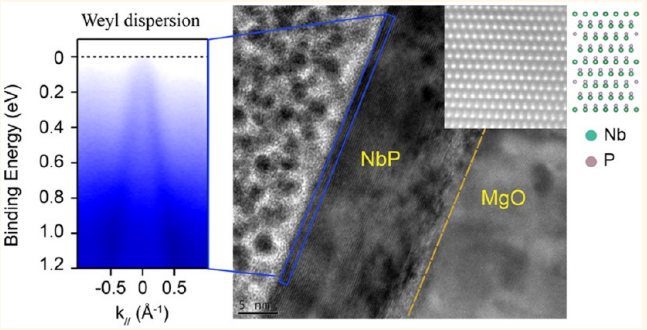

KEYWORDS: *weyl semimetal thin films, transition metal monopnictides, type-I weyl semimetals, molecular beam epitaxy, weyltronics*

Weyl semimetals, materials with symmetry-protected gapless electronic bands in which electrons obey the physics of Weyl fermions, are one of the current most exciting topics in topological matter.[1,2] The existence of Weyl fermions was first predicted in material breaking time-reversal symmetry such as pyrochlore iridates,[3] but their experimental realization was achieved in compound breaking inversion symmetry, the transition metal monopnictides.[4−12] So far, these compounds were synthesized as bulk single crystals in the structural space group $I4_1md$ and with the composition MX (M = Nb, Ta, X = P, As). Their identification as Weyl semimetals relies on the observation of characteristic features in their electronic structure: a linear dispersion with band crossings (Weyl points) and Fermi-arcs in the surface states have been conclusively measured by several groups using angle-resolved photoemission spectroscopy[6−11] and further confirmed by local spectroscopic techniques.[13−16] Moreover, the coupling of Weyl fermions to external electromagnetic fields results in the nonconservation of chiral charges—the so-called Adler−Jackiw anomaly.[17] Signatures of this chiral anomaly have been investigated in magnetotransport experiments, with some concerns regarding the possible role of inhomogeneous current flow in bulk crystals.[18−20] While major efforts have been put into microstructuring bulk crystals by focused-ion beam milling,[21−25] thereby enabling advanced thermal transport[21] and nonlinear optical measurements,[25] fabrication-related issues appear when approaching the thin film limit. In this context, the realization of a bottom-up approach to synthesize Weyl semimetals would be helpful, making nonlocal transport experiments[26] a viable route. Furthermore, thin film growth would allow the control of the topological properties of WSMs via doping or strain, a parameter space that cannot be explored with the present bulk crystals. Strain gradients in a WSM crystal are expected to induce electromagnetic gauge fields,[27] leading to the observation of emergent phenomena such as landau levels and quantum oscillations in the absence of an applied magnetic field[28] and a quantization of the circular photogalvanic effect.[29] Moreover, there have been a number of fundamental phenomena in WSM thin films addressed by theory, such as

Received: December 19, 2019
Accepted: February 13, 2020
Published: February 13, 2020

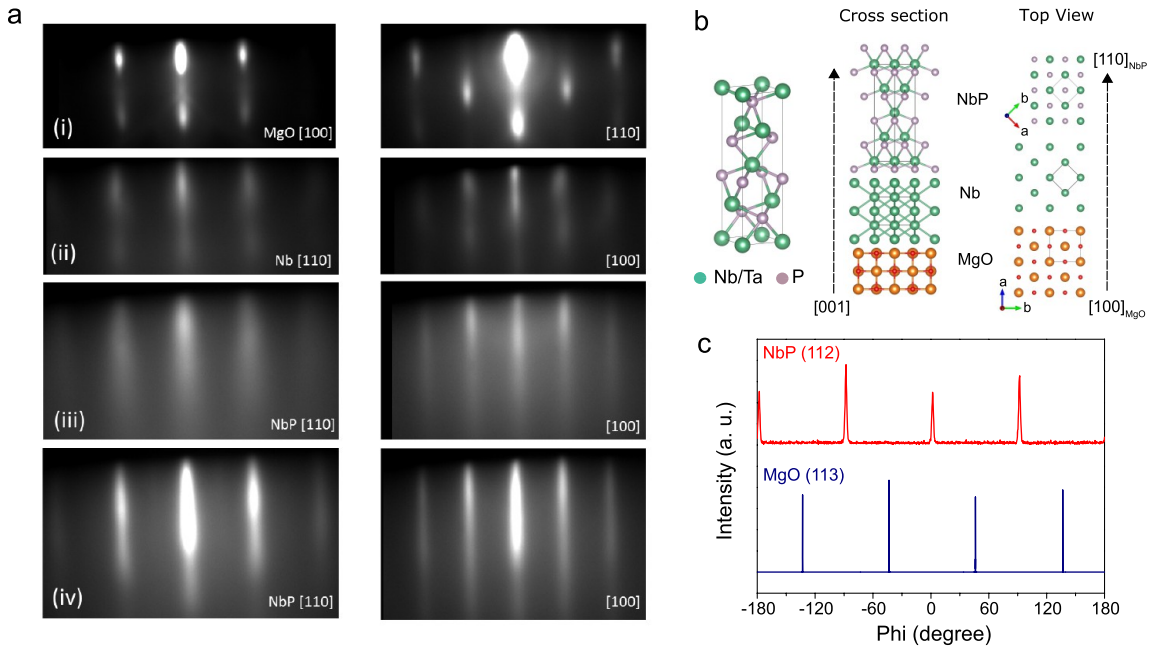

Figure 1. (a) Evolution of the RHEED pattern during NbP epitaxial growth: (i) MgO substrate, (ii) Nb-buffer layer, (iii) phosphorization of the Nb surface and formation of the first NbP monolayer, and (iv) NbP growth. (b) Sketch of the NbP/TaP structure and epitaxial relationship among the substrate, buffer layer, and film. (c) X-ray diffraction Phi-scan of the NbP (112) and MgO (113) reflections, indicating a 4-fold symmetric, single-crystalline oriented growth rotated by 45° with respect to the substrate.

an unusual twisting of the Fermi surface,[30] the emergence of Floquet topological insulator phases,[31] a metal−insulator transition upon thickness confinement,[32] or even a special interplay of long- and short-range surface plasmon-polariton modes.[33] On the other hand, promising application areas of WSMs have been addressed, pointing to them as efficient hydrogen catalysts,[34] colossal photovoltaic materials,[25] mid-infrared detectors,[35] and most recently, topological magnets.[36−39] But the most important implication of WSM thin films is the possibility to fabricate atomically engineered heterostructures and functional interfaces. It allows the interplay of WSMs with other materials, such as superconductors, (anti)ferromagnetic, or ferroelectric materials, to be explored. In this respect, there have been exciting predictions of interfacial effects that make WSMs appealing for spintronic and superconducting devices, such as a large topology-driven spin-Hall[40] and Edelstein effects,[41] as well as a chirality-dependent Josephson current.[42] It is thus clear that the fabrication of thin films will boost the impact of WSMs both in the fundamental and applied research perspectives.

In this article, we report the growth of NbP and TaP thin films on insulating MgO(100) substrates by molecular-beam epitaxy. Both phosphide compounds have been conclusively shown to be type-I Weyl semimetals in the bulk crystal form by angle-resolved photoemission experiments.[8−11] Our epitaxial layers present clear differences with respect to the bulk crystals: (i) both in-plane and out-of plane lattice parameters are larger by more than 1%, (ii) the composition of the films is slightly in the P-rich regime, and (iii) the film surfaces exhibit sub-unit cell steps (2.8 Å) that point to a single surface termination. The resulting electronic properties are marked by a downward shift of the Fermi energy (0.2 eV) below the calculated intrinsic E_F, which effectively increases the carrier density due to multiple band crossings. Furthermore, a phosphorus-terminated surface is naturally achieved by the growth method and is consistent with the nature of the topological surface states in both experiment and calculations. The successful realization of epitaxial thin films will allow for the use of strain and controlled doping to tailor the electronic structure of Weyl semimetals, paving the way towards the fabrication of functional WSM heterostructures.

RESULTS AND DISCUSSION

The NbP (TaP) compounds crystallize in the $I4_1md$ structural space group, which is a tetragonal lattice with parameters a = 3.34 Å (3.36 Å) and c = 11.37 Å (11.41 Å). The method of choice for epitaxial growth is to use the basal (a−b) plane of the pnictide structure to match with substrates with a cubic structure, i.e., to grow the films along the (001) direction. However, for a reasonable lattice matching on typical cubic oxide insulators, the NbP (TaP) growth has to be stabilized with an in-plane rotation of 45° in the basal plane with respect to the substrate. To this end, MgO (100) substrates were selected and prepared *ex situ* to achieve an atomically flat surface prior to growth (more details about the substrate choice can be found in Supporting Information Note 1). Figure 1a summarizes the growth strategy with the help of *in situ* reflection high energy electron diffraction (RHEED) patterns: (i) we start from an atomically flat MgO (100) surface, (ii) a subsequent growth of a thin Nb (Ta) (001) buffer layer, (iii) the phosphorization of the metal buffer layer, and finally (iv) the overgrowth of the phosphide layer. This procedure results in a very streaky NbP (TaP) RHEED pattern indicative of a quasi layer-by-layer growth. From the analysis of the diffraction patterns, it is evident that the Nb (Ta) buffer layer grows 45° rotated with respect to the MgO substrate in the basal plane, following the epitaxial relationship MgO [100]//Nb [110] and MgO[110]//Nb[100] (see structural models in Figure 1b for clarity). After completion of the buffer layer, the Nb surface is exposed to a controlled phosphorus atmosphere, until high-order streaks (twice the distance of the

https://dx.doi.org/10.1021/acsnano.9b09997
ACS Nano 2020, 14, 4405−4413

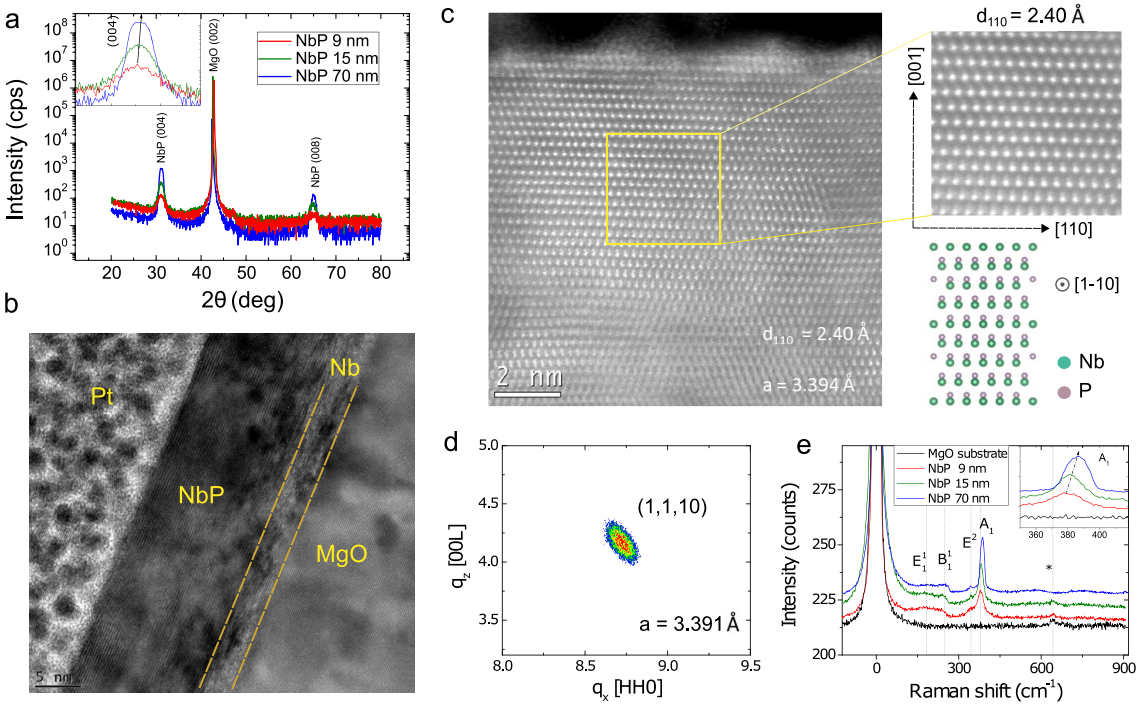

Figure 2. (a) X-ray diffraction (θ–2θ scan) of NbP thin films, indicating a (001) oriented film with the absence of secondary phases. (b) Transmission electron microscopy overview image of a MgO/Nb (2 nm)/NbP (15 nm) cross-section. A Pt protection layer has been placed during TEM sample preparation. (c) High-resolution STEM images of the NbP film region in the [1$\bar{1}$0] direction, resolving the crystal structure and the location of the Nb and P atoms in the lattice. (d) Reciprocal space mapping of the (1,1,10) reflection of the same NbP film studied by TEM. The extracted in-plane lattice parameters match with the local TEM determination, confirming the large-scale homogeneity of the films. (e) Thickness dependent Raman spectra of the NbP thin films. The shift of the A_1 mode toward higher frequencies is highlighted in the inset.

main streaks in reciprocal space) appear. This observation is consistent with the formation of a NbP monolayer that is shifted by $a/2$ with respect to the buffer layer, which is inherent to the structure of NbP along the growth direction (c-axis; see cross-section in Figure 1b). The Nb-surface phosphorization is another crucial step to guarantee a smooth NbP overgrowth: streaky RHEED patterns indicative of flat epitaxial NbP layers are observed reproducibly with the adopted growth strategy. It should be noted that periodic RHEED reflections are only visible in the high symmetry directions, while there are no coherent patterns at intermediate angles, indicating that the NbP (TaP) films grow with a single-crystalline orientation without twinning/twisting of in-plane crystalline domains. *Ex situ* X-ray diffraction measurements (Figure 1c) corroborate the single-crystalline order: a sharp 90° periodicity in the film peaks is observed upon azimuthal rotation (Phi-scan). Furthermore, by plotting the Phi-scans of the film and the substrate together, it is shown that the epitaxial relationship (45° rotation in-plane) does not change throughout the whole film thickness.

Figure 2 shows a detailed investigation of the structural properties, comprising X-ray diffraction (XRD), high-resolution scanning transmission electron microscopy (S-TEM), and Raman spectroscopy. A standard θ–2θ scan taken on NbP films of various thicknesses (9–70 nm) shows only (004) and (008) NbP reflections (Figure 2a), confirming an epitaxial, single crystalline oriented growth without secondary phases. While the X-ray reflection pattern from the Nb buffer layer cannot be resolved due to the reduced thickness (2–5 nm), it can be well visualized in the overview cross-sectional TEM image in Figure 2b. As anticipated in the RHEED patterns during growth, the Nb buffer layer has a certain degree of structural disorder, which is not present in the NbP layers grown on top. The fine details of the structure are shown in Figure 2c, where a high-resolution high-angle annular dark field (HAADF) STEM image of the NbP film in the [110] direction displays highly ordered in- and out-of-plane lattice planes, with an excellent matching to the NbP structural model. The lattice planes are particularly visible by the high atomic contrast of the Nb atoms, while a faint contrast corresponding to the light P atoms can be distinguished in the zoomed-in image (Figure 2c, right panel) at the expected atomic positions. Taking advantage of the excellent structural order, a line intensity profile of the atomic rows has been taken to calculate the average in-plane lattice parameter of the NbP film (Supporting Information Figure S1). For the [110] direction, a Nb–Nb atom distance of 2.40 Å has been inferred, which results in an in-plane lattice parameter a = 3.394 Å. In order to compare the quantification using both local and global methods, a reciprocal space mapping (RSM) X-ray diffraction scan has been performed on the (1,1,10) reflection of NbP (Figure 2d), yielding an in-plane lattice parameter of a = 3.391 Å, an excellent agreement within the error of the TEM linescan averaging and the determination of the XRD intensity maxima. The in-plane lattice parameters do not vary as the thickness is varied from 15 to 70 nm according to the RSM measurements (see Supporting Information Figure S2), which means that the films do not change the in-plane strain state in the studied thickness range. On the other hand, the out-of-plane lattice parameters extracted from the (004) peak positions (inset of

https://dx.doi.org/10.1021/acsnano.9b09997
ACS Nano 2020, 14, 4405–4413

Figure 2a) decrease only very slightly (11.50 Å to 11.46 Å) with increasing thickness. The negligible thickness dependence of both in-plane and out-of-plane parameters suggests that the films grow fully relaxed from the very early stage. Interestingly, the lattice parameters (a = 3.39 Å, c = 11.48 Å) sizably differ from the bulk crystal values (a = 3.34 Å, c = 11.37 Å), which means that a bigger unit cell is stabilized during the layer-by-layer growth on the MgO(001)/Nb(001) surface. Figure 2e shows the thickness-dependent Raman spectra of NbP thin films. Besides the elastic peak, the characteristic vibrational modes (E_1, B_1, E_2, A_1) are observed, which correspond to the NbAs structure type (space group $Im4c$). The most prominent peak belongs to the A_1 mode (around 380 cm^{-1}) while the other modes present a much lower intensity, in agreement with the reported bulk spectra and theoretical calculations.[43] We observe a small redshift of the A_1 mode as the thickness of the films increases (inset of Figure 2e), which arises due to the slightly smaller c-lattice parameter found on thicker films. While in ref 43, the redshift was measured by applying hydrostatic pressure, in our case it was achieved by the thickness-dependent epitaxy. Thus, the shift of the A_1 mode can be used as a quick tool to probe the strain in the films, an important parameter for tuning the electronic properties of WSMs. Besides, unlike X-ray diffraction, Raman scattering is able to map different fingerprints for the isostructural NbP and TaP compounds, as evidenced in the frequency shift of the B^1 mode (Supporting Information Figure S3). It is also worth noting that the asymmetry of the Raman line shape and its temperature dependence (not measured here) has been recently found to give insights into electron−phonon coupling in type-I WSM systems,[44] calling for future studies in the thin film regime.

The chemical composition and valence states of the NbP (TaP) thin films have been studied by *in situ* X-ray photoemission spectroscopy (XPS). The details of the Nb 3d 5/2 and P 2p core level spectra (Figure 3a,b) show that Nb and P shift in opposite directions compared to the neutral Nb^0 and P^0 valence state, consistent with the expected chemical shifts due to electron transfer in the NbP compound (Nb^{III} and P^V valence). The stoichiometry of the films has been determined using the area under the curve of the core levels with the respective sensitivity factors, yielding a slightly P-rich ($Nb_{0.49}P_{0.51}$) composition. Complementary to XPS, which is a surface sensitive technique, the in-depth composition of the films has been studied by Rutherford backscattering spectroscopy (RBS). The best fitting to the spectra (Figure 3c) yields a 47.6% to 52.4% (Nb:P) composition, indicating that the P-rich composition is distributed homogeneously across the full NbP layer. Similar results with regard to bonding-related core-level shifts and P-rich composition have been found in TaP layers (Supporting Information Figure S4). A real-space visualization of the layer homogeneity is further shown by energy-dispersive X-ray spectroscopy along a 15 nm NbP cross section (Figure 3d).

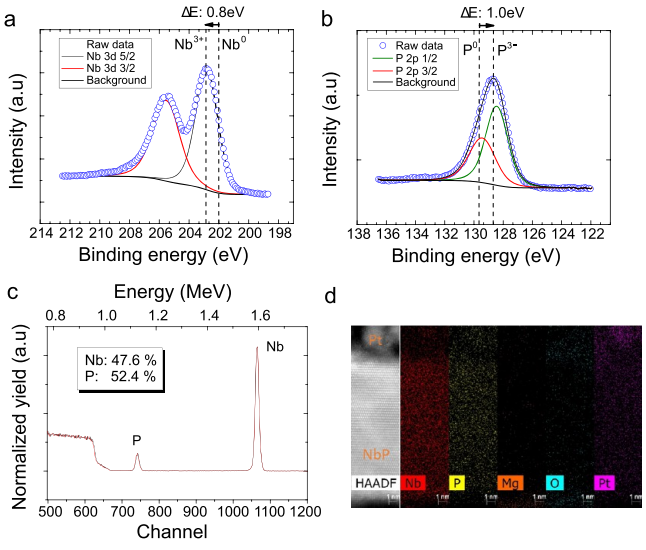

Figure 3. (a, b) In situ X-ray photoelectron spectroscopy of Nb 3d and P 2p core levels of NbP, highlighting the energy shifts in opposite directions due to chemical bonding. (c) Rutherford backscattering spectra of a 20 nm thick NbP sample. The red curve is the fit for composition determination. (d) Energy dispersive X-ray spectra on a TEM cross section, showing a homogeneous distribution of Nb and P species along the film thickness.

The topography and surface structure of NbP and TaP films is of paramount importance for the observation of topological surface states (Fermi-arcs) and has been thus investigated by scanning probe microscopy (Figure 4 and Supporting Information Figure S5). Large-scale atomic force microscopy images (Supporting Information Figure S5a) reveal a flat topography, yielding root-mean-square (RMS) roughness values of 0.43 nm. The grain size varies from 50 to 100 nm showing regions of grain coalescence, whereas the intergrain steps correspond mostly to 1 unit cell height. In order to investigate the topography inside and between the grains, *in situ* scanning tunneling microscopy images have been acquired (Figure 4). Square and rectangular shaped grains can be identified with two preferred orientations, along 45° and −45° on the image axis (i.e., along (100) direction), consistent with the 4-fold in-plane crystal symmetry of NbP. A closer look to the grain topography reveals the presence of atomically flat terraces. The height of each step terrace amounts to 2.8 Å, corresponding to 1/4 unit cell fractions (a single Nb−P monolayer), as depicted in Figure 4b (a structural model of the NbP unit cell along the growth direction (001) is drawn as a guide to the eye). We rarely find slight deviations of exact unit cell fractions, which might arise if adjacent grains end in a different (Nb/P) atomic termination or due to the presence of intergrain stacking faults. From the topography statistics, a predominantly single surface termination (either Nb or P) scenario is likely to happen throughout the film surface. Figure 4c,d shows a zoomed-in topography image comparing NbP and TaP film surfaces, the latter having a smaller terrace width. Additional scanning tunneling spectra (STS) have been acquired on a flat region (marked with a square in Figure 4d) and reveal a parabolic behavior with a finite density of states at zero bias, characteristic of metallic systems. An enhanced conductance (shoulder) is observed around +0.2 V bias voltage, which points to a larger electronic density of states above the Fermi energy (unoccupied states).

Having assessed the properties of the film surface, momentum-resolved photoemission spectra have been taken using an in-house designed and built momentum microscope[45] with a He−I light source (see Methods for details). Figure 5 summarizes the overall electronic structure of a 15 nm-thick NbP thin film measured at 100 K, including Fermi-surface topology and band dispersion along relevant (Weyl point) cuts, together with *ab initio* calculations using the experimentally obtained unit cell parameters. At the Fermi-energy

https://dx.doi.org/10.1021/acsnano.9b09997
ACS Nano 2020, 14, 4405−4413

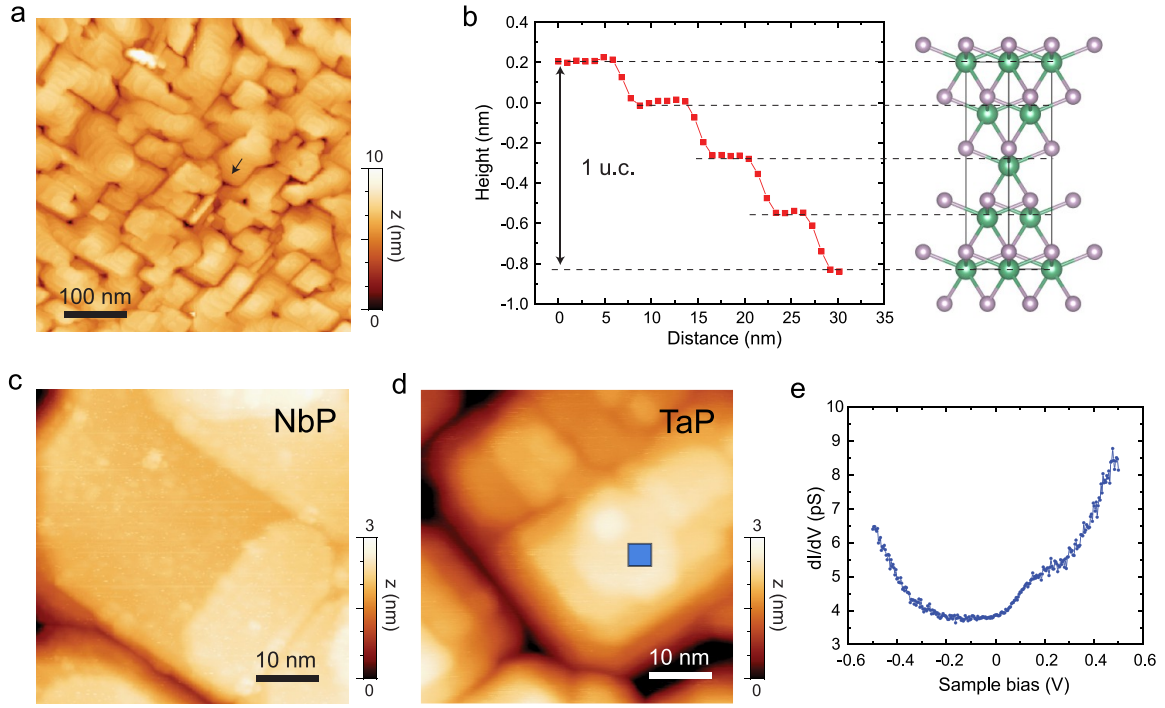

Figure 4. (a) Overview scanning tunneling microscopy image (500 nm × 500 nm, V = 1 V, I = 2 pA) of a 20 nm-thick NbP film, revealing rectangular grains oriented along the (100) direction (45° in the image) with atomically flat terraces. (b) Height profile across a NbP grain (marked with an arrow in panel a), featuring terrace steps of 2.8 Å, which correspond to a NbP monolayer (1/4 u.c.). The NbP unit cell in the (001) direction is drawn next to it as guide for the eye. (c, d) Zoomed-in topography images of NbP (V = 1 V, I = 2 pA) and TaP (V = 0.3 V, I = 10 pA), respectively. The terrace size in the TaP films appears to be smaller. (e) Scanning tunneling spectrum (STS) (V = 0.5 V, I = 10 pA) of a TaP epitaxial grain (marked as a square in panel d) revealing a finite density of states at zero-bias and a parabolic behavior with an enhanced conductance around 0.2 V.

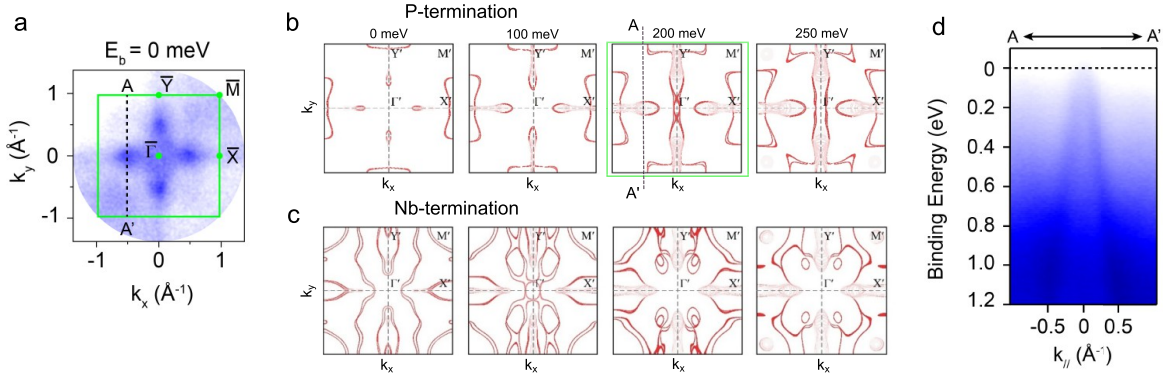

Figure 5. Electronic structure of the NbP thin films (t = 15 nm) revealed by momentum-resolved photoemission spectroscopy. (a) Constant energy contour at zero binding energy (Fermi surface). The green square represents the Brillouin zone (BZ). (b, c) *Ab initio* calculations of constant-energy contours (surface projection) at different binding energies for a P-terminated (panel b) and Nb-terminated surfaces (panel c), respectively. The calculated energy contours of the P-termination at a 200 meV binding energy (highlighted in green) match well with the experimental results at E_F, evidencing a Fermi-level shift in the as-grown film. (d) Energy dispersion along the A−A′ direction (defined in panel a), which corresponds to the cut across the Weyl point projection (k_x = 0.54 Å^{-1}).[11,12] A linear dispersion is clearly observed.

(E_b = 0 meV), four electronic pockets with an elliptic shape directed toward the X and Y symmetry points can be identified, as shown in Figure 5a. A detailed comparison with the calculation of the termination-dependent surface states (Figure 5b,c) reveals that the elliptic and cross-like band features along Γ−X and Γ−Y are characteristic of the P-terminated NbP surface states (the features for a Nb termination are radically different). Interestingly, the size and shape of the measured elliptical (also called spoon-like) features at E_F match with the calculations and the bulk crystal data in refs 10 , 11 , and 46 only when an energy shift of ΔE = −0.2 eV (E_b = 200 meV) is considered (highlighted in a green box, Figure 5b), suggesting an effective hole doping in the as-grown thin films. Figure 5d shows the energy dispersion cut along A → A′, which is expected to cross the location of one pair of Weyl points in NbP (k_x = 0.54 Å^{-1}, E_b = −0.026 eV) and thus used to visualize the surface Fermi arcs.[10,11] A clear linear band dispersion is observed, in agreement with previous photoemission results of cleaved monopnictide bulk crystals.[6−11] This dispersion originates from the Fermi-arcs, but their k_x−k_y contour at the Weyl points cannot be mapped in our NbP films due to the E_F shift (−0.2 eV) with respect to the intrinsic

https://dx.doi.org/10.1021/acsnano.9b09997
ACS Nano 2020, 14, 4405−4413

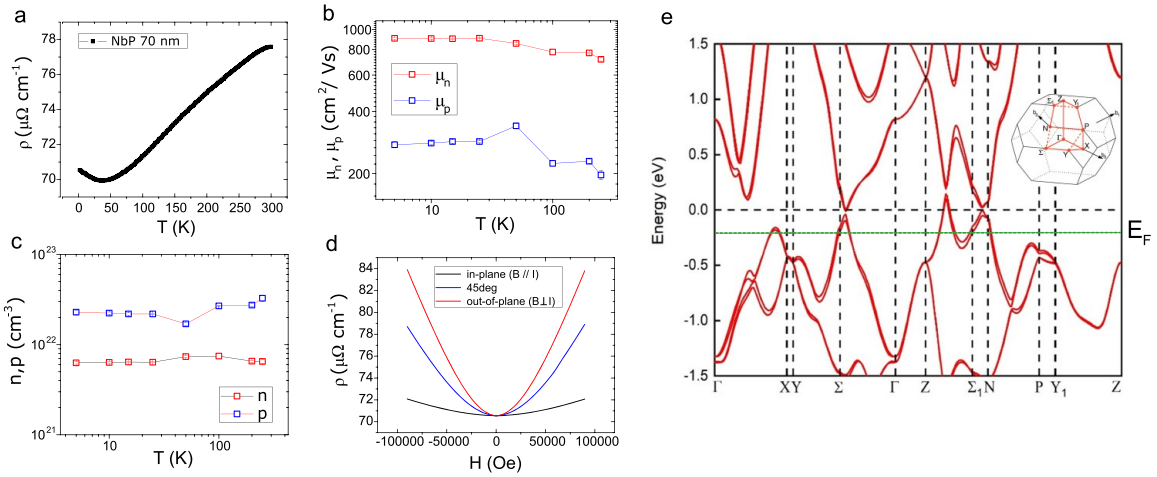

Figure 6. Electrical and magnetotransport properties of NbP films and their relation to the bulk band structure. (a) Temperature dependence of the resistivity of a 70 nm-thick NbP film. In this thickness regime, the parallel buffer layer conduction (t = 2 nm) is negligible. (b) Electron and hole mobility calculated using the two-carrier model, exhibiting a very shallow temperature dependence. (c) Carrier density dependence revealing holess as majority carriers throughout the measured temperature range. (d) Angular dependent magnetoresistance, exhibiting positive MR dependence under both in and out-of-plane magnetic fields (absence of chiral anomaly). (e) Bulk band structure calculations of NbP showing all the relevant bands inside the Brillouin zone, and highlighting the presence of multiple hole pockets at the experimentally determined E_F (green line), in agreement with the large hole concentration (>10^{22} cm^{-3}) obtained by the Hall effect.

Fermi level, and second, due the intrinsically short separation of the Weyl points in momentum space (Δk < 0.05 Å^{-1}) for the NbP compound, a detection challenge even for high-resolution synchrotron ARPES.[10,11,46] It is noteworthy that only these topological surface states (elliptic shape, A → A′ cut) are observed in our films, whereas the bowtie features centered at the X and Y points) are completely absent. This merits further investigation and will be discussed elsewhere. On the other hand, the origin of the effective hole-doping in the as-grown thin films can be attributed to residual acceptors (Nb-vacancies) arising from the MBE growth process, in agreement with the slightly P-rich composition of the films inferred by XPS and RBS. The strained lattice parameters of the phosphide thin films will also have an effect on the Fermi-level position. Although we estimate that the effect of the lattice parameters (∼1% tensile strain) is rather small, further studies are needed to disentangle the contribution from strain and vacancy acceptors on E_F, in order to get a full understanding of Fermi-level engineering of Weyl semimetals achieved by epitaxial design.

Finally, electrical transport measurements have been analyzed only for thick films (t = 70 nm), so that shunting effects of the thin buffer layer can be discarded. The temperature dependence of the resistivity (Figure 6a) shows the expected metallic behavior for NbP.[47] We do not observe superconductivity down to 2 K, in contrast to recent reports on platelets formed from bulk crystals using focused ion beam milling.[24] The carrier density in the as-grown films has been extracted by standard Hall effect measurements, and as already anticipated from the Fermi-level shift determined by photoemission (ΔE = −0.2 eV), both electron and hole bands will contribute to electronic transport. Thus, slightly nonlinear transverse resistances (R_{xy}) as a function of the magnetic field have been fitted by the two-carrier model to extract the densities of the electrons (n_e) and holes (n_p), as well as the electron (μ_e) and hole (μ_p) mobilities as a function of temperature, summarized in Figure 6b,c. Being energetically 0.2 eV below the Weyl points, the density of states at E_F encompasses mainly hole-like bands, as shown in the bulk band structure calculations (Figure 6e), and thus the majority carriers are holes with a carrier density (10^{21}– 10^{22} cm^{-3}) higher than in the bulk crystals (10^{20} cm^{-3}).[47] The resulting electron (hole) mobilities are close to 900 cm^2/(V s) (300 cm^2/(V s)) and feature a weak temperature dependence similar to heavily doped (degenerate) semiconductors. Moreover, a positive magnetoresistance is observed both for in-plane (B // I) and out-of plane (B ⊥ I) magnetic fields, suggesting the absence of chiral anomaly in the as-grown films. This result corroborates that the chiral anomaly is highly sensitive to the location of the Fermi energy (E_F = −0.2 eV). The effect of chiral charge pumping is strongly diminished away from the Weyl points, due to the contribution of nontopological bands at other locations in momentum space (see Figure 6e). At high magnetic fields, a linear, nonsaturating behavior of the resistivity sets in (Supporting Information Figure S6), typically observed in high-mobility compensated semimetals.

CONCLUSION

In summary, epitaxial thin films of type-I Weyl semimetals NbP and TaP have been synthesized via molecular beam epitaxy. A rigorous structural, morphological, and chemical characterization was carried out to assess the quality of the films. During the epitaxial growth process, the layers are stabilized with a larger lattice constant (1%) and with a slight P-rich stoichiometry with respect to the bulk crystals. The excellent surface quality, featuring a homogeneous P-termination, allows the visualization of topological surface states with a linear dispersion. A Fermi-level shift of around −0.2 eV with respect to the intrinsic E_F is determined by comparing the photoemission spectra with *ab initio* calculations and bulk crystal data; and arises mainly due to the formation of Nb-vacancy acceptors (P-rich conditions). The realization of high-quality WSM thin films and the intimate relation between strain, doping, band structure, and electronic transport discussed here constitutes a route to access and control topological states in order to design functional heterostructures and Weyltronic devices.

https://dx.doi.org/10.1021/acsnano.9b09997
ACS Nano 2020, 14, 4405−4413

METHODS

Substrate Preparation and Molecular-Beam Epitaxy Growth. MgO (100) substrates were soaked in methanol for 20 min and rinsed with water followed by annealing in O_2 atmosphere (1150 °C) for 3.5 h to achieve an atomically flat surface prior to film growth. The typical substrate dimensions are 5 × 10 mm. Nb (Ta) rods are evaporated via electron-beam heating, and P species are thermally evaporated from a GaP compound effusion cell in a custom-made UHV chamber (p_{base} = 1 × 10^{-10} mbar), with a regeneration system for residual P_2 (red) and P_4 (white phosphorus). The GaP compound cell is employed to reduce the amount of pyrolytic white phosphorus upon evaporation (P_2/P_4 ∼ 100). A cross-beam mass spectrometer (XBS Hiden) is used to calibrate the atomic fluxes and monitor the amount of P_2/P_4 species. No Ga species have been detected under evaporation conditions (T_{cell} = 850 °C). The substrate temperature is controlled by radiation heating. The Nb (Ta) buffer layer is grown at 300 °C, at a rate of 3−5 nm/h and a pressure of p = 4 × 10^{-10} mbar. The surface of the buffer layer is then exposed to a P_2 flux (BEP: 1 × 10^{-8} mbar) to achieve phosphorization, whereas the subsequent NbP (TaP) layer is grown under P-rich conditions (Nb:P flux 1:20), a moderate substrate temperature (300−400 °C), and a slow rate (<4 nm/h), controlled by the Nb (Ta) flux. The thicknesses of the films presented in this work range between 9 and 70 nm. After concluding the growth process, the sample is cooled down very slowly (10 °C/min) to room temperature under P atmosphere (p = 1 × 10^{-8} mbar), to ensure a homogeneous P-termination at the surface.

***In Situ* Characterization.** The crystallinity of the films is monitored *in situ* by reflection high energy electron diffraction (RHEED), using a 15 kV electron beam. The layers are further characterized by *in situ* tools (XPS, STM, and momentum microscope) with the use of a vacuum suitcase transfer system (Ferrovac, p_{base} < 1 × 10^{-10} mbar) to move the as-deposited film under UHV conditions from the growth to the analysis chambers. Core-level X-ray photoelectron spectra (XPS) were taken at room temperature using Al Kα radiation and a hemispherical analyzer. The STM experiments were performed on an Omicron VT-STM-XT system operated at room temperature with a base pressure of 2 × 10^{-11} mbar. The mechanically sharpened Pt/Ir tips were treated and checked on the Au(111) surface before measurements, and the topography images were acquired at room temperature. A sinusoidal modulation of 30 mV and 713 Hz was added to the bias voltage for the measurements of dI/dV spectra. Momentum-resolved photoemission spectra were acquired using an in-house designed momentum microscope,[45] using a helium lamp ($h\nu$ = 21.2 eV), at 100 K and with an energy step of 10 meV.

***Ex Situ* Characterization.** X-ray diffraction patterns, including reciprocal space maps, were taken in a commercial 4-circle diffractometer (Bruker) using Cu Kα radiation. Transmission electron microscopy (TEM) was carried out in an aberration corrected high-resolution microscope (FEI, Titan). Cross-sectional lamellas of the MgO/Nb/NbP stack (t = 100 nm) were prepared by focused ion beam (FIB) with Ga-ion etching. A Pt protection layer is deposited on the sample before lifting the lamella to the TEM grid. Raman spectra were acquired using a 532 nm excitation wavelength at room temperature. Rutherford backscattering spectroscopy using particle induced X-ray emission was measured using a 1.9 MV alpha+ beam at a 169° scattering angle in an NEC Pelletron accelerator.

Device Fabrication and Electrical Transport. Hall-bar devices were patterned using laser-assisted optical lithography (Heidelberg Instruments) and etched via an Ar-discharge plasma (500 V DC) under high-vacuum conditions. Cr/Au (4 nm/80 nm) contacts were deposited by DC magnetron sputtering. The device sizes ranged from (5 × 15) μm^2 (width × length) to (100 × 300) μm^2 (aspect ratio 1:3).

***Ab Initio* Calculations.** Electronic structure calculations are performed within the density functional theory as implemented in the Vienna *ab initio* simulation package (VASP).[48,49] The exchange-correlation energy is treated within the Perdew−Burke−Ernzerhof (PBE) parametrization[50] of the generalized gradient approximation. The kinetic energy cutoff for the plane wave basis is 300 eV, and a k-mesh of 500 × 500 × 1 is adopted for the Brillouin zone integration. A six-unit-cell thick slab model is constructed by cutting NbP along the (001) plane of the conventional cell, and the in-plane cell size is 1 × 1 for the conventional cell. The internal coordinates of the atoms in the surface unit cell are fully relaxed. Spin−orbit coupling is considered in the electronic structure calculations. All the surface band structures and Fermi surfaces are projected onto the atoms in the surface unit cell of the P- and Nb-termination, accordingly.

ASSOCIATED CONTENT

Supporting Information

The Supporting Information is available free of charge at https://pubs.acs.org/doi/10.1021/acsnano.9b09997.

Complementary information about the determination of lattice parameters by TEM and RSM, comparison of NbP and TaP thin films by XRD and Raman spectroscopy, chemical and compositional analysis of TaP thin films, and surface structure by AFM and temperature-dependent magnetotransport, as well as a Supplementary Note about the substrate choice (PDF)

AUTHOR INFORMATION

Corresponding Authors

Amilcar Bedoya-Pinto − *Max Planck-Institute of Microstructure Physics 06120 Halle, Saale, Germany*; Email: abedoya@mpi-halle.mpg.de

Stuart S. P. Parkin − *Max Planck-Institute of Microstructure Physics 06120 Halle, Saale, Germany*; orcid.org/0000-0003-4702-6139; Email: stuart.parkin@mpi-halle.mpg.de

Authors

Avanindra Kumar Pandeya − *Max Planck-Institute of Microstructure Physics 06120 Halle, Saale, Germany*

Defa Liu − *Max Planck-Institute of Microstructure Physics 06120 Halle, Saale, Germany*

Hakan Deniz − *Max Planck-Institute of Microstructure Physics 06120 Halle, Saale, Germany*

Kai Chang − *Max Planck-Institute of Microstructure Physics 06120 Halle, Saale, Germany*

Hengxin Tan − *Max Planck-Institute of Microstructure Physics 06120 Halle, Saale, Germany*

Hyeon Han − *Max Planck-Institute of Microstructure Physics 06120 Halle, Saale, Germany*; orcid.org/0000-0002-2973-5225

Jagannath Jena − *Max Planck-Institute of Microstructure Physics 06120 Halle, Saale, Germany*

Ilya Kostanovskiy − *Max Planck-Institute of Microstructure Physics 06120 Halle, Saale, Germany*

Complete contact information is available at: https://pubs.acs.org/10.1021/acsnano.9b09997

Author Contributions

A.B.-P. and S.S.P.P. conceived the project. A.B.-P. customized the MBE system, developed the film growth strategy, prepared the films, and performed sample characterization and data analysis (RHEED, XRD, Raman, Electrical transport). A.K.P assisted with the film growth and carried out XPS measurements, device fabrication, and data analysis (XPS, 2-carrier model). D.L. performed the momentum-resolved photoemission measurements and data analysis. H.T. calculated the bulk band structure and termination-dependent surface states. H.D. carried out the TEM measurements, and J.J.

https://dx.doi.org/10.1021/acsnano.9b09997
ACS Nano 2020, 14, 4405−4413

prepared the cross-section lamella by FIB. K.C. carried out the STM/STS measurements and data analysis. H.H. performed the RSM measurements/Phi-scans and data analysis. I.K. carried out the RBS measurements and data analysis. A.B.-P. wrote the manuscript with contributions of all of the authors. S.S.P.P. supervised the entire project.

Notes

The authors declare no competing financial interest.
A preprint version of this article is available in *arXiV*.[51]

ACKNOWLEDGMENTS

We thank G. Woltersdorf and C. Koerner (MLU Halle) for their assistance regarding Raman measurements, Y. Sun (MPI-CPfS) for theoretical input, and P. Sessi for critical reviewing of the manuscript. D.L. thanks the Alexander von Humboldt Foundation for support.

REFERENCES

(1) Armitage, N. P.; Mele, E. J.; Vishwanath, A. Weyl and Dirac Semimetals in Three-Dimensional Solids. *Rev. Mod. Phys.* **2018**, *90*, 015001.
(2) Jia, S.; Xu, S.-Y.; Hasan, M. Z. Weyl Semimetals, Fermi Arcs and Chiral Anomalies. *Nat. Mater.* **2016**, *15*, 1140−1144.
(3) Wan, X.; Turner, A. M.; Vishwanath, A.; Savrasov, S. Y. Topological Semimetal and Fermi-Arc Surface States in the Electronic Structure of Pyrochlore Iridates. *Phys. Rev. B: Condens. Matter Mater. Phys.* **2011**, *83*, 205101.
(4) Xu, S.-Y.; Belopolski, I.; Alidoust, N.; Neupane, M.; Bian, G.; Zhang, C.; Sankar, R.; Chang, G.; Yuan, Z.; Lee, C.-C.; Huang, S.-M.; Zheng, H.; Ma, J.; Sanchez, D. S.; Wang, B.; Bansil, A.; Chou, F.; Shibayev, P. P.; Lin, H.; Jia, S.; Hasan, M. Z. Discovery of a Weyl Fermion Semimetal and Topological Fermi Arcs. *Science* **2015**, *349*, 613−617.
(5) Lv, B. Q.; Weng, H. M.; Fu, B. B.; Wang, X. P.; Miao, H.; Ma, J.; Richard, P.; Huang, X. C.; Zhao, L. X.; Chen, G. F.; Fang, Z.; Dai, X.; Qian, T.; Ding, H. Experimental Discovery of Weyl Semimetal TaAs. *Phys. Rev. X* **2015**, *5*, 031013.
(6) Yang, L. X.; Liu, Z. K.; Sun, Y.; Peng, H.; Yang, H. F.; Zhang, T.; Zhou, B.; Zhang, Y.; Guo, Y. F.; Rahn, M.; Prabhakaran, D.; Hussain, Z.; Mo, S.-K.; Felser, C.; Yan, B.; Chen, Y. Weyl Semimetal Phase in the Non-Centrosymmetric Compound TaAs. *Nat. Phys.* **2015**, *11*, 728−732.
(7) Lv, B. Q.; Xu, N.; Weng, H. M.; Ma, J. Z.; Richard, P.; Huang, X. C.; Zhao, L. X.; Chen, G. F.; Matt, C. E.; Bisti, F.; Strocov, V.; Mesot, J.; Fang, Z.; Dai, X.; Qian, T.; Shi, M.; Ding, H. Observation of Weyl Nodes in TaAs. *Nat. Phys.* **2015**, *11*, 724−727.
(8) Xu, N.; Weng, H.; Lv, B.; Matt, C.; Park, J.; Bisti, F.; Strocov, V.; Gawryluk, D.; Pomjakushina, E.; Conder, K.; Plumb, N.; Radovic, M.; Autes, G.; Yazyev, O.; Fang, Z.; Dai, X.; Qian, T.; Mesot, J.; Ding, H.; Shi, M. Observation of Weyl Nodes and Fermi Arcs in Tantalum Phosphide. *Nat. Commun.* **2016**, *7*, 11006.
(9) Xu, S.-Y.; Beloposki, I.; Sanchez, D.; Zhang, C.; Chang, G.; Guo, C.; Bian, G.; Yuan, Z.; Lu, H.; Chang, T.-R.; Shibayev, P.; Prokopovych, M.; Alidoust, N.; Zheng, H.; Lee, C.-C.; Huang, S.-M.; Sankar, R.; Chou, F.; Hsu, C.-H.; Jeng, H.-T.; et al. Experimental Discovery of a Topological Weyl Semimetal State in TaP. *Sci. Adv.* **2015**, *1*, No. e1501092.
(10) Souma, S.; Wang, Z.; Kotaka, H.; Sato, T.; Nakayama, K.; Tanaka, Y.; Kimizuka, H.; Takahashi, T.; Yamauchi, K.; Oguchi, T.; Segawa, K.; Ando, Y. Direct Observation of Nonequivalent Fermi-Arc States of Opposite Surfaces in the Noncentrosymmetric Weyl Semimetal NbP. *Phys. Rev. B: Condens. Matter Mater. Phys.* **2016**, *93*, 161112.
(11) Liu, Z. K.; Yang, L. X.; Sun, Y.; Zhang, T.; Peng, H.; Yang, H. F.; Chen, C.; Zhang, Y.; Guo, Y. F.; Prabhakaran, D.; Schmidt, M.; Hussain, Z.; Mo, S.-K.; Felser, C.; Yan, B.; Chen, Y. Evolution of the Fermi Surface of Weyl Semimetals in the Transition Metal Pnictide Family. *Nat. Mater.* **2016**, *15*, 27−31.
(12) Lee, C. C.; Xu, S. Y.; Huang, S. M.; Sanchez, D. S.; Belopolski, I.; Chang, G.; Bian, G.; Alidoust, N.; Zheng, H.; Neupane, M.; Wang, B.; Bansil, A.; Hasan, Z.; Lin, H. Fermi Surface Interconnectivity and Topology in Weyl Fermion Semimetals TaAs, TaP, NbAs, and NbP. *Phys. Rev. B: Condens. Matter Mater. Phys.* **2015**, *92*, 235104.
(13) Sessi, P.; Sun, Y.; Bathon, T.; Glott, F.; Li, Z.; Chen, H.; Guo, L.; Chen, X.; Schmidt, M.; Felser, C.; Yan, B.; Bode, M. Impurity Screening and Stability of Fermi Arcs against Coulomb and Magnetic Scattering in a Weyl Monopnictide. *Phys. Rev. B: Condens. Matter Mater. Phys.* **2017**, *95*, 035114.
(14) Inoue, H.; Gyenis, A.; Wang, Z.; Li, J.; Oh, S. W.; Jiang, S.; Ni, N.; Bernevig, A.; Yazdani, A. Quasiparticle Interference of the Fermi Arcs and Surface-Bulk Connectivity of a Weyl Semimetal. *Science* **2016**, *351*, 1184−1187.
(15) Batabyal, R.; Morali, N.; Avraham, N.; Sun, Y.; Schmidt, M.; Felser, C.; Stern, A.; Yan, B.; Beidenkopf, H. Visualizing Weakly Bound Surface Fermi Arcs and Their Correspondence to Bulk Weyl Fermions. *Sci. Adv.* **2016**, *2*, No. e1600709.
(16) Zheng, H.; Chang, G.; Huang, S. M.; Guo, C.; Zhang, X.; Zhang, S.; Yin, J.; Xu, S. Y.; Belopolski, I.; Alidoust, N.; Sanchez, D.; Bian, G.; Chang, T.-R.; Neupert, T.; Jeng, H.-T.; Jia, S.; Lin, H.; Hasan, Z. Mirror Protected Dirac Fermions on a Weyl Semimetal NbP Surface. *Phys. Rev. Lett.* **2017**, *119*, 196403.
(17) Adler, S. L. Axial-Vector Vertex in Spinor Electrodynamics. *Phys. Rev.* **1969**, *177*, 2426−2438.
(18) Reis, R. D. D.; Ajeesh, M. O.; Kumar, N.; Arnold, F.; Shekhar, C.; Naumann, M.; Schmidt, M.; Nicklas, M.; Hassinger, E. On the Search for the Chiral Anomaly in Weyl Semimetals: The Negative Longitudinal Magnetoresistance. *New J. Phys.* **2016**, *18*, 085006.
(19) Yang, J. J.; Zhen, W. L.; Liang, D. D.; Wang, Y. J.; Yan, X.; Weng, S. R.; Wang, J. R.; Tong, W.; Pi, L.; Zhu, W. K.; Zhang, C. J. Current Jetting Distorted Planar Hall Effect in a Weyl Semimetal with Ultrahigh Mobility. *Phys. Rev. Mater.* **2019**, *3*, 014201.
(20) Liang, S.; Lin, J.; Kushwaha, S.; Xing, J.; Ni, N.; Cava, R. J.; Ong, N. P. Experimental Tests of the Chiral Anomaly Magnetoresistance in the Dirac-Weyl Semimetals Na_3Bi and GdPtBi. *Phys. Rev. X* **2018**, *8*, 031002.
(21) Gooth, J.; Niemann, A.; Meng, T.; Grushin, A.; Landsteiner, K.; Gotsmann, B.; Menges, F.; Schmidt, M.; Shekhar, C.; Suess, V.; Huehne, R.; Rellinghaus, B.; Felser, C.; Yan, B.; Nielsch, K. Experimental Signatures of the Mixed Axial−gravitational Anomaly in the Weyl Semimetal NbP. *Nature* **2017**, *547*, 324−327.
(22) Niemann, A. C.; Gooth, J.; Wu, S. C.; Bäßler, S.; Sergelius, P.; Hühne, R.; Rellinghaus, B.; Shekhar, C.; Süß, V.; Schmidt, M.; Felser, C.; Yan, B.; Nielsch, K. Chiral Magnetoresistance in the Weyl Semimetal NbP. *Sci. Rep.* **2017**, *7*, 43394.
(23) Bachmann, M. D.; Nair, N.; Flicker, F.; Ilan, R.; Meng, T.; Ghimire, N. J.; Bauer, E. D.; Ronning, F.; Analytis, J. G.; Moll, P. J. W. Inducing Superconductivity in Weyl Semimetal Microstructures by Selective Ion Sputtering. *Sci. Adv.* **2017**, *3*, No. e1602983.
(24) van Delft, M. R.; Pezzini, S.; König, M.; Tinnemans, P.; Hussey, N. E.; Wiedmann, S. Surface and Bulk Superconductivity at Ambient Pressure in the Weyl Semimetal TaP. *arXiV*, 09702, 2018. https://arxiv.org/abs/1808.09702 (August 28, 2018).
(25) Osterhoudt, G. B.; Diebel, L. K.; Gray, M. J.; Yang, X.; Stanco, J.; Huang, X.; Shen, B.; Ni, N.; Moll, P. J. W.; Ran, Y.; Burch, K. Colossal Mid-Infrared Bulk Photovoltaic Effect in a Type-I Weyl Semimetal. *Nat. Mater.* **2019**, *18*, 471−475.
(26) Parameswaran, S. A.; Grover, T.; Abanin, D. A.; Pesin, D. A.; Vishwanath, A. Probing the Chiral Anomaly with Nonlocal Transport in Three-Dimensional Topological Semimetals. *Phys. Rev. X* **2014**, *4*, 031035.
(27) Pikulin, D. I.; Chen, A.; Franz, M. Chiral Anomaly from Strain-Induced Gauge Fields in Dirac and Weyl Semimetals. *Phys. Rev. X* **2016**, *6*, 041021.

https://dx.doi.org/10.1021/acsnano.9b09997
ACS Nano 2020, 14, 4405−4413

(28) Liu, T.; Pikulin, D. I.; Franz, M. Quantum Oscillations without Magnetic Field. *Phys. Rev. B: Condens. Matter Mater. Phys.* **2017**, *95*, 041201.
(29) De Juan, F.; Grushin, A. G.; Morimoto, T.; Moore, J. E. Quantized Circular Photogalvanic Effect in Weyl Semimetals. *Nat. Commun.* **2017**, *8*, 15995.
(30) Bovenzi, N.; Breitkreiz, M.; O'Brien, T. E.; Tworzydło, J.; Beenakker, C. W. J. Twisted Fermi Surface of a Thin-Film Weyl Semimetal. *New J. Phys.* **2018**, *20*, 023023.
(31) Chen, R.; Xu, D. H.; Zhou, B. Floquet Topological Insulator Phase in a Weyl Semimetal Thin Film with Disorder. *Phys. Rev. B: Condens. Matter Mater. Phys.* **2018**, *98*, 235159.
(32) Taherinejad, M.; Spaldin, N. Metal-Insulator Transition in Weyl Semimetal Thin Films. *APS March Meeting Abstracts*; 2018; E10.010.
(33) Tamaya, T.; Kato, T.; Tsuchikawa, K.; Konabe, S.; Kawabata, S. Surface Plasmon Polaritons in Thin Film Weyl Semimetals. *J. Phys.: Condens. Matter* **2019**, *31*, 305001.
(34) Rajamathi, C. R.; Gupta, U.; Kumar, N.; Yang, H.; Sun, Y.; Süß, V.; Shekhar, C.; Schmidt, M.; Blumtritt, H.; Werner, P.; Yan, B.; Parkin, S.; Felser, C.; Rao, C. Weyl Semimetals as Hydrogen Evolution Catalysts. *Adv. Mater.* **2017**, *29*, 1606202.
(35) Chan, C. K.; Lindner, N. H.; Refael, G.; Lee, P. A. Photocurrents in Weyl Semimetals. *Phys. Rev. B: Condens. Matter Mater. Phys.* **2017**, *95*, 041104.
(36) Liu, E.; Sun, Y.; Kumar, N.; Muechler, L.; Sun, A.; Jiao, L.; Yang, S. Y.; Liu, D.; Liang, A.; Xu, Q.; Kroder, J.; Süß, V.; Borrmann, H.; Shekhar, C.; Wang, Z.; Xi, C.; Wang, W.; Schnelle, W.; Wirth, S.; Chen, Y.; et al. Giant Anomalous Hall Effect in a Ferromagnetic Kagome-Lattice Semimetal. *Nat. Phys.* **2018**, *14*, 1125−1131.
(37) Liu, D. F.; Liang, A. J.; Liu, E. K.; Xu, Q. N.; Li, Y. W.; Chen, C.; Pei, D.; Shi, W. J.; Mo, S. K.; Dudin, P.; Kim, T.; Cacho, C.; Li, G.; Sun, Y.; Yang, L.; Liu, Z.; Parkin, S.; Felser, C.; Chen, Y. Magnetic Weyl Semimetal Phase in a Kagomé Crystal. *Science* **2019**, *365*, 1282−1285.
(38) Morali, N.; Batabyal, R.; Nag, P. K.; Liu, E.; Xu, Q.; Sun, Y.; Yan, B.; Felser, C.; Avraham, N.; Beidenkopf, H. Fermi-Arc Diversity on Surface Terminations of the Magnetic Weyl Semimetal $Co_3Sn_2S_2$. *Science* **2019**, *365*, 1286−1291.
(39) Belopolski, I.; Manna, K.; Sanchez, D. S.; Chang, G.; Ernst, B.; Yin, J.; Zhang, S. S.; Cochran, T.; Shumiya, N.; Zheng, H.; Singh, B.; Bian, G.; Multer, D.; Chang, T.-R.; Xu, S.-Y.; Bansil, A.; et al. Discovery of Topological Weyl Fermion Lines and Drumhead Surface States in a Room Temperature Magnet. *Science* **2019**, *365*, 1278−1281.
(40) Sun, Y.; Zhang, Y.; Felser, C.; Yan, B. Strong Intrinsic Spin Hall Effect in the TaAs Family of Weyl Semimetals. *Phys. Rev. Lett.* **2016**, *117*, 146403.
(41) Johansson, A.; Henk, J.; Mertig, I. Edelstein Effect in Weyl Semimetals. *Phys. Rev. B: Condens. Matter Mater. Phys.* **2018**, *97*, 085417.
(42) Zhang, S. B.; Erdmenger, J.; Trauzettel, B. Chirality Josephson Current Due to a Novel Quantum Anomaly in Inversion-Asymmetric Weyl Semimetals. *Phys. Rev. Lett.* **2018**, *121*, 226604.
(43) Gupta, S. N.; Singh, A.; Pal, K.; Muthu, D. V. S.; Shekhar, C.; Qi, Y.; Naumov, P. G.; Medvedev, S. A.; Felser, C.; Waghmare, U. V.; Sood, A. Pressure-Induced Lifshitz Transition in NbP: Raman, X-Ray Diffraction, Electrical Transport, and Density Functional Theory. *Phys. Rev. B: Condens. Matter Mater. Phys.* **2018**, *97*, 064102.
(44) Coulter, J.; Osterhoudt, G. B.; Garcia, C. A. C.; Wang, Y.; Plisson, V. M.; Shen, B.; Ni, N.; Burch, K. S.; Narang, P. Uncovering Electron-Phonon Scattering and Phonon Dynamics in Type-I Weyl Semimetals. *Phys. Rev. B: Condens. Matter Mater. Phys.* **2019**, *100*, 220301.
(45) Tusche, C.; Krasyuk, A.; Kirschner, J. Spin Resolved Bandstructure Imaging with a High Resolution Momentum Microscope. *Ultramicroscopy* **2015**, *159*, 520−529.
(46) Belopolski, I.; Xu, S. Y.; Sanchez, D. S.; Chang, G.; Guo, C.; Neupane, M.; Zheng, H.; Lee, C. C.; Huang, S. M.; Bian, G.; Alidoust, N.; Chang, T.-R.; Wang, B.; Zhang, X.; Bansil, A.; Jeng, H.-T.; Lin, H.; Jia, S.; Hasan, M. Criteria for Directly Detecting Topological Fermi Arcs in Weyl Semimetals. *Phys. Rev. Lett.* **2016**, *116*, 066802.
(47) Shekhar, C.; Nayak, A. K.; Sun, Y.; Schmidt, M.; Nicklas, M.; Leermakers, I.; Zeitler, U.; Skourski, Y.; Wosnitza, J.; Liu, Z.; Chen, Y.; Schnelle, W.; Borrmann, H.; Grin, Y.; Felser, C.; Yan, B. Extremely Large Magnetoresistance and Ultrahigh Mobility in the Topological Weyl Semimetal Candidate NbP. *Nat. Phys.* **2015**, *11*, 645−649.
(48) Kresse, G.; Furthmüller, J. Efficiency of *Ab-Initio* Total-Energy Calculations for Metals and Semiconductors Using a Plane-Wave Basis Set. *Comput. Mater. Sci.* **1996**, *6*, 15.
(49) Kresse, G.; Furthmüller, J. Efficient Iterative Schemes for *Ab Initio* Total-Energy Calculations Using a Plane-Wave Basis Set. *Phys. Rev. B: Condens. Matter Mater. Phys.* **1996**, *54*, 11169.
(50) Perdew, J. P.; Burke, K.; Ernzerhof, M. Generalized Gradient Approximation Made Simple. *Phys. Rev. Lett.* **1996**, *77*, 3865.
(51) Bedoya-Pinto, A.; Pandeya, A. K.; Liu, D.; Deniz, H.; Chang, K.; Tan, H.; Han, H.; Jena, J.; Kostanovskiy, I.; Parkin, S. Towards Weyltronics: Realization of Epitaxial NbP and TaP Weyl Semimetal Thin Films, 2019, *arXiV*. https://arxiv.org/abs/1909.12707 (September 27, 2019).

https://dx.doi.org/10.1021/acsnano.9b09997
ACS Nano 2020, 14, 4405−4413